

Article

# Effect of Boron and Oxygen on the Structure and Properties of Protective Decorative Cr–Al–Ti–N Coatings Deposited by Closed Field Unbalanced Magnetron Sputtering (CFUBMS)

Ph. V. Kiryukhantsev-Korneev , Zh. S. Amankeldina, A. N. Sheveyko, S. Vorotilo and E. A. Levashov

National University of Science and Technology “MISIS”, Leninsky Prospect, 4, 119049 Moscow, Russia; zhazira.amankeldina@mail.ru (Z.S.A.); sheveyko@mail.ru (A.N.S.); s.vorotilo@misis.ru (S.V.); levashov@shs.misis.ru (E.A.L.)

\* Correspondence: kiruhancev-korneev@yandex.ru

Received: 1 October 2019; Accepted: 14 November 2019; Published: 19 November 2019



**Abstract:** Boron and oxygen-doped Cr–Al–Ti–N coatings were deposited by closed field unbalanced magnetron sputtering (CFUBMS) of TiB target manufactured by self-propagating high-temperature synthesis, and Ti, Cr, and Al targets. To evaluate the influence of doping elements, as-deposited coatings were studied by glow discharge optical emission spectroscopy (GDOES), SEM, XRD, and optical profilometry. Mechanical properties were measured by nanoindentation and tribological, abrasive and electrochemical testing. The introduction of boron suppresses columnar growth and leads to structural refinement and a decrease of coating’s surface roughness. The addition of 2.3 at.% boron results in the highest mechanical properties: hardness  $H = 15$  GPa, stable friction coefficient  $f = 0.65$ , and specific wear  $Vw = 7.5 \times 10^{-6} \text{ mm}^3\text{N}^{-1}\text{m}^{-1}$ . To make the coating more visually appealing, oxygen was introduced in the chamber near the end of the deposition cycle. Upper Cr–Al–Ti–B–O–N layers were studied in terms of their composition and coloration, and the developed two-layer decorative coatings were deposited on cast metallic art pieces.

**Keywords:** Cr–Al–Ti–B–O–N coatings; TiB target; unbalanced magnetron sputtering; CFUBMS; composition and structure; hardness and elastic modulus; wear; abrasive and corrosion resistance; friction coefficient; decorative properties

## 1. Introduction

During the lifetime of art pieces, the pieces’ surfaces experience a plethora of negative effects, including corrosion, friction, and abrasive wear. In particular, cast brass is susceptible to oxidation, scratching and loss of luster. One way to protect such art pieces and expand their lifespan is the application of two-layered protective ion plasma-deposited coatings. In such coatings, the lower layer provides mechanical stability, and the upper layer serves the decorative purpose. In terms of mechanical properties and wear resistance, transitional metal-nitride coatings doped with boron are particularly attractive.

The development of novel coatings based on transition metal nitrides (including the boron-alloyed ones) is relevant for the increase of performance and lifespan of various items, including cutting tools [1–3], pressing tools [4,5], frictional units [6,7], microelectronic elements [8–10], optical devices [11,12], medical implants [13], magnetic recording devices [14], etc.

A variety of techniques can be used for the deposition of coatings based on nitrides and borides of transitional metals. Chemical vapor deposition (CVD) provides the benefit of high uniformity of

coatings even on complex-shaped parts [15]. However, the application of CVD is restricted if the substrate material is sensitive to overheating. Since the heating of the substrate is necessary for the CVD processes, this deposition technique cannot be efficiently used for parts made of brass, bronze, aluminum-based alloys, etc. Atomic-layer deposition (ALD) produces coatings with outstanding depth uniformity, even in holes, grooves, and other hard-to-access areas [16–18]. However, the ALD technique is incapable of depositing thick coatings. Closed field unbalanced magnetron sputtering (CFUBMS) is one of the most suitable techniques for the deposition of transitional metal nitride-based coatings, especially on temperature-sensitive substrates [19,20]. Increased field strength enhances the plasma ionization and provides higher ion currents on the substrate [21]. As a result, dense coatings are formed at lower substrate temperatures and offset voltage.

TiN is the most ubiquitous industrial coating due to its high corrosion resistance, thermophysical properties, and hardness (20–40 GPa depending on deposition parameters) [22]. CrN coatings are also frequently used due to their lower wear rate and higher fracture toughness, which result in superior wear resistance [23]. Ternary nitride coatings can provide even higher mechanical properties and wear resistance, as exemplified by Ti–Cr–N (40 GPa), Ti–Al–N (25–35 GPa), Cr–Ti–N (16 GPa), and Cr–Al–N (17 GPa) [24]. Gradient Cr/CrN/Cr–Ti–Al–N coatings demonstrated especially high hardness (35 GPa) and adhesion strength [25].

Doping of nitride-based coatings by boron produces nanocomposite (nc) structures with anomalously high hardness (50 GPa) [26], good wear resistance and low friction coefficient [27,28], high oxidation resistance, and thermal stability [29,30]. Max hardness (50 GPa) for nc-TiN/a-BN and nc-TiN/a-BN/a-TiB<sub>2</sub> coatings was achieved when TiN grains (25–30 and ≤10 nm, correspondingly) were separated by near-monoatomic layers of a-BN [31]. Doping of CrN by boron produces two types of nanocomposite structures: nc-CrN/a-BN [28,32] and nc-CrB<sub>2</sub>/a-BN [33]. Seventeen to 43 GPa hardness was reported for Cr–B–N coatings [34–39]. Such coatings are usually deposited by reactive PVD in Ar + N<sub>2</sub> atmosphere using CrB<sub>2</sub> or CrB targets.

Boron doping for CFUBMS coatings was investigated mainly for the ternary Ti–B–N and Cr–B–N coatings [40–43]. Presumably, boron doping of more complex Cr–Al–Ti–N coating might provide considerable improvement in microstructural and mechanical aspects.

When applied to cast art pieces, the coating should provide suitable coloration of the upper layer. This might be conveniently achieved by the introduction of oxygen in the deposition chamber near the end of the deposition cycle.

The goal of this study was to evaluate the effects of boron doping on the structure and properties of protective Cr–Al–Ti–N coatings deposited by CFUBMS both on soft, temperature-sensitive substrate (cast brass) and more robust substrates (monocrystalline silicon and stainless steel), and to investigate the influence of deposition parameters (deposition duration and oxygen flow) on the chemical composition and decorative properties of the upper Cr–Al–Ti–B–O–N layer of the coating.

## 2. Materials and Methods

Discs (Ø 30 × 5 mm) and pendants (40 × 20 × 2) were made from LS 59-1 grade brass by investment casting and used as substrates along with rectangular plates of monocrystalline (111) KEF-4.5 solar silicon and 12H18N10T steel. Cr–Al–Ti–B–N coatings were deposited using a UDP 850/4 magnetron sputtering device equipped with a CFUBMS system (Teer Coatings Ltd., Droitwich, UK). The elemental composition of the coatings was based on our previously published investigation of quaternary Cr–Al–Ti–N coatings with various contents of metallic components [44]. Deposition was carried out at ~0.2 Pa pressure in Ar (99.998%) + N<sub>2</sub> (99.999%) atmosphere using four 90 mm × 690 mm targets: Ti (99.99%), Al (99.99%), Cr (99.99%), TiB (81.6% Ti + 18.4% B). The TiB target (SHIM-4 grade) was manufactured by force SHS pressing.

Before the deposition, all targets were conditioned for 10 min at 5 A current and 30 cm<sup>3</sup>/min Ar flow. To increase the adhesion and reduce the strain on the surface-coating interface, a thin Cr inter-layer was deposited in the Ar atmosphere. Al target was sputtered in impulse regime with

frequency  $\nu = 50$  kHz and impulse duration  $T = 200$  microseconds. During the deposition of the Cr–Al–Ti–B–N layer, the Ar/N<sub>2</sub> flow was 30/30 cm<sup>3</sup>/min. Various currents (0; 0.5; 1; 1.5; 3; 5 A) were applied to the TiB target. All other targets were supplied with a constant 5 A current to prevent the over-heating and deterioration of brass substrates. The deposition duration was 90 min. During the deposition, substrates were rotated five times per minute. The residual pressure in the chamber was  $2.6 \times 10^{-4}$  Pa. Cr–Al–Ti–B–N coatings were marked as «P1-6» (protective).

To deposit the upper decorative Cr–Al–Ti–B–O–N layer, nitrogen was substituted by air in the supplied reactive gas mixture. Cr–Al–Ti–B–O–N coatings were marked as «D1-9» (decorative). The deposition process was preliminarily optimized in terms of gas flow and rotational speed. Chemical composition and element distribution profiles across the thickness of the coating were studied by glow discharge optical emission spectroscopy (GDOES) using Profiler 2 installation (“Horiba Jobin Yvon”, Longjumeau Cedex, France). Microstructural analysis of the transverse fractures of coatings was performed on scanning electron microscope JSM-7600F (JEOL, Tokyo, Japan), equipped with the Oxford energy dispersive spectroscopy add-on. X-ray diffraction analysis (XRD) was performed on Bruker D8 installation using the monochromatic CuK $\alpha$  radiation. Hardness ( $H$ ), Young modulus ( $E$ ) and elastic recovery ( $W$ ) were measured by instrumental indentation at 4 mN load using Nano Hardness Tester (CSM Inst., Peseux, Switzerland) equipped with a Berkovich indenter. Tribometer (CSM Inst., Switzerland) was used for “pin-on-disc” tribological testing at an applied load of 1 N, 200 m distance and 10 cm/s linear velocity. Al<sub>2</sub>O<sub>3</sub> ball ( $d = 6$  mm) was used as a counterpart.

Coatings’ abrasive resistance was estimated using a calowear-tester (NIITAvtoprom, Moscow, Russia). The 100Cr6 steel ball ( $d = 27$  mm) was used as a counterpart material. The slurry containing 15- $\mu$ m-sized diamond particles (Struers) was applied to the sample surface before tests. During the test duration (5 min), constant load (0.5 N) and ball rotation speed (153 rotations per minute) were applied.

Coatings deposited onto LS 59-1 brass were subjected to sliding wear and abrasion testing. To ascertain the specific wear and abrasion impact, specimens were studied using optical profilometer Veeco WYKO NT1100 (Veeco, Plainview, NY, USA). Electrochemical testing was performed on potentiostat Voltalab PST050 (Radiometr analytical, Lyon, France) in a thermostatic electrochemical cell equipped with AgCl comparative electrode, Lugin capillary and a secondary 1 cm<sup>2</sup> Pt electrode. Measurements were performed in a 1N H<sub>2</sub>SO<sub>4</sub> solution.

### 3. Results

Table 1 provides the depth-averaged GDOES data for elemental compositions of coatings deposited on brass. Six groups of Cr–Al–Ti–B–N coatings were deposited. The deposition rate was  $\sim 30$  nm/min. All elements were distributed evenly across the coating’s thickness of 3–4  $\mu$ m (Figure 1). In the B-free coating, the N content is below the saturation, e.g., 43.5% of N. However, the nitride’s non-metallic sublattice probably also contains the oxygen and carbon, i.e., N + O + C = 48.3%, which is closer to stoichiometry. To avoid possible confusion, it should be noted that two sources of Ti atoms were used for deposition: TiB and Ti targets. Therefore, the coatings contained titanium even when the sputtering current on the TiB target was 0. An increase in the current supplied to the TiB target from 0 to 0.5 A led to higher concentrations of boron and lower concentrations of nitrogen in the coatings. It also somewhat decreased the measured Ti/Al ratio in the coating. This apparent increase in aluminum content is probably caused by the conditioning of the targets and formation of interlayers. The boundaries of interlayers are not clearly defined, and the signal from the interlayer might have got mixed into the calculation of average concentration values.

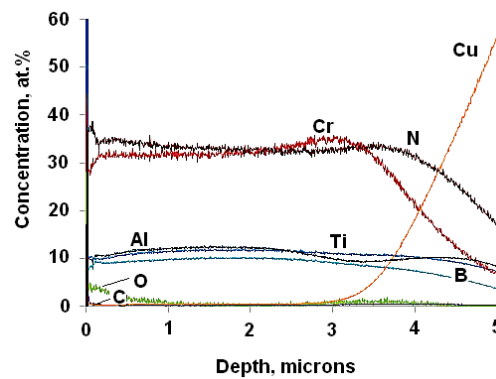


Figure 1. Profiles of elements' distribution across the thickness of coating with 10 at.% B.

Table 1. Chemical composition and width of Cr–Al–Ti–B–N coatings.

Specimen	$I_{TiB}$ , A	Elemental Composition, at.%							Coating Thickness, $\mu\text{m}$
		Cr	Al	Ti	B	N	O	C	
P1	0	38.9	8.6	4.2	0	43.5	4.3	0.5	3.5
P2	0.5	38.0	14.6	5.1	0.4	38.7	2.4	0.8	3.5
P3	1	41.0	11.6	6.1	2.0	38.1	1.0	0.2	3.0
P4	1.5	35.0	16.1	8.5	2.3	35.2	2.4	0.5	3.0
P5	3	35.5	12.7	10.2	7.3	33.0	0.3	0.1	4.0
P6	5	33.5	12.0	11.7	10.0	32.0	0.5	0.2	3.5

SEM images of transverse fractures of Cr–Al–Ti–B–N coatings deposited on Si (100) are provided in Figure 2. The addition of 2 at.% boron (coating P 3) to Cr–Al–Ti–N coating gradually suppressed the formation of a columnar structure and decreased the diameter of columns from 90–100 to 40–50 nm. This effect was dependent on boron concentration. At 10 at.% B, a dense uniform structure with nearly equiaxial grains was formed.

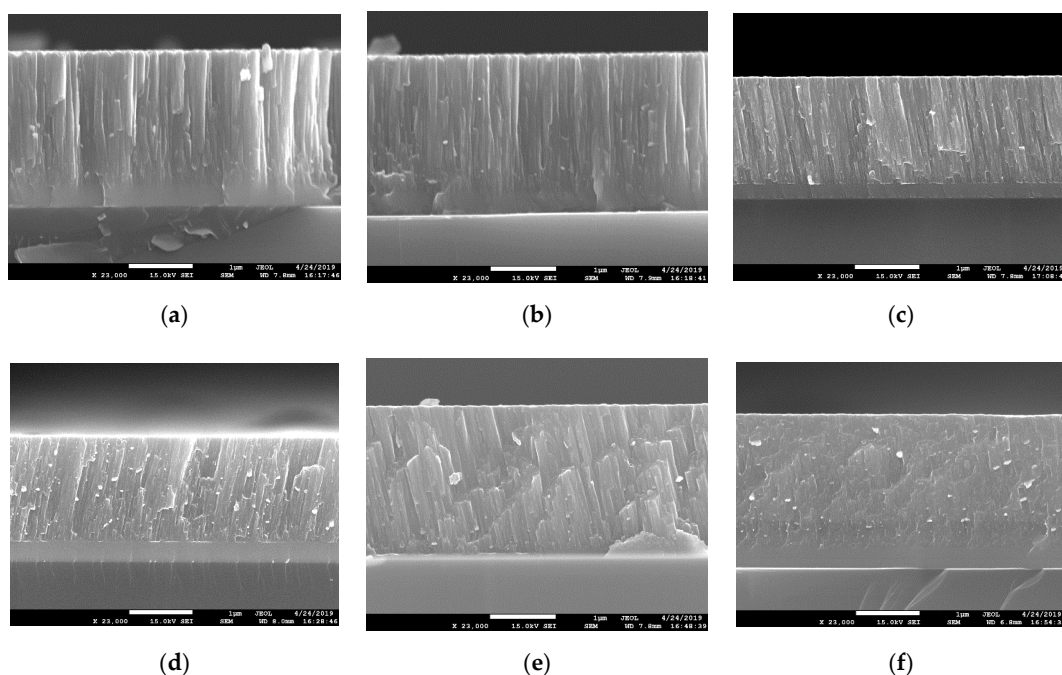


Figure 2. SEM images of fractured Cr–Al–Ti–B–N coatings: (a) 0 at.% B, (b) 0.4 at.% B, (c) 2 at.% B, (d) 2.3 at.% B, (e) 7.3 at.% B, (f) 10 at.% B.

XRD patterns (Figure 3) feature pronounced peaks at  $2\theta = 70^\circ$ , which correspond to the Si substrate. FCC CrN-related peaks (111), (200), (220), (311) were located at  $2\theta = 38.6^\circ$ ;  $44.8^\circ$ ;  $65.6^\circ$ ; and  $82.8^\circ$ . TiN peaks (111), (200), (220), and (311) TiN were detected at  $2\theta = 37^\circ$ ;  $41^\circ$ ;  $63.3^\circ$ ; and  $78.1^\circ$ . AlN was not detected, suggesting the complete dissolution of aluminum in CrN and TiN. Coatings with 0–2.3 at.% feature no peaks of boron-based phases. Coatings with 7.3 at.% were X-ray amorphous, so no discrete peaks of nitride or boride phases could be discerned. A further increase of B content prompted the formation of the  $\text{CrB}_2$ -based phase with a peak at  $2\theta = 33.9^\circ$ .

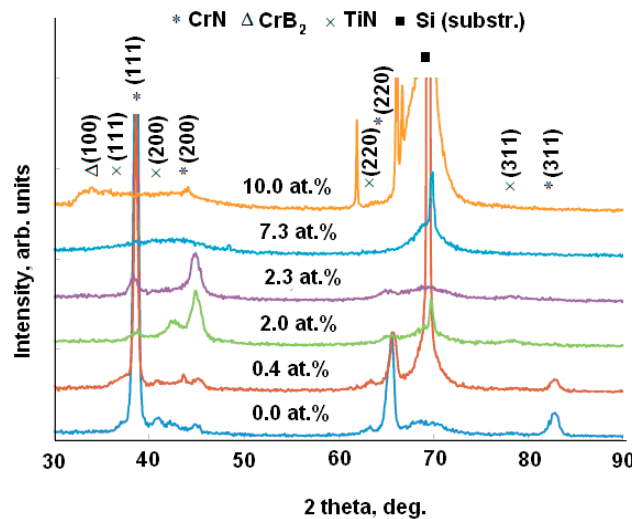


Figure 3. XRD patterns for the Cr–Al–Ti–B–N coatings.

Crystallite sizes were calculated from peaks' broadening using the Scherrer's formula. The size of CrN crystallites calculated using (111), (200), (220), and (311) peaks was 17–19 nm in the boron-free coatings and decreased to 9–16 nm upon introduction of 2–2.3 at.% B in the coating. The size of TiN crystallites estimated on the basis of (111), (200), and (220) peaks in the baseline coatings and in the coatings with 0.4 at.% boron was  $d = 30$ – $50$  nm and was reduced by 40% in the coatings with 2 and 2.3% B ( $d = 13$ – $28$  nm). Coating P5 with 7.3% boron was X-ray amorphous. Coating with 10 at.% B had a fine structure, but the estimation of crystallite size was complicated by the overlapping of peaks on the related XRD pattern.

Lattice parameters for FCC CrN were  $a = 0.405$ – $0.410$  nm, which is considerably lower as compared to the standard value (0.414 nm). The lattice parameter for TiN was  $a = 0.423 \pm 0.001$  nm, which is relatively close to the standard of 0.424 nm.

Nanoindentation data was used to plot the dependence of hardness ( $H$ ), Young modulus ( $E$ ), elastic recovery ( $W$ ), as well as of  $H/E$  and  $H^3/E^2$  ratios on the boron content (Figure 4). Coatings P3 and P4 containing 2 and 2.3 at.% B were characterized by the max hardness  $H = 15$  GPa, which decreased with the growing B concentration. The boron-free coating was characterized by relatively low hardness  $H = 10.4$  GPa and elastic recovery  $W = 0.47$ , but possessed high Young modulus  $E = 190$  GPa.  $H/E$  and  $H^3/E^2$  ratios for the investigated coatings were also highest for the coatings with a boron content of 2.3 at.% and decreased with further boron enrichment. Therefore, hardness and elastic-plastic characteristics were maximal for the coatings with 2 and 2.3 at.% B.

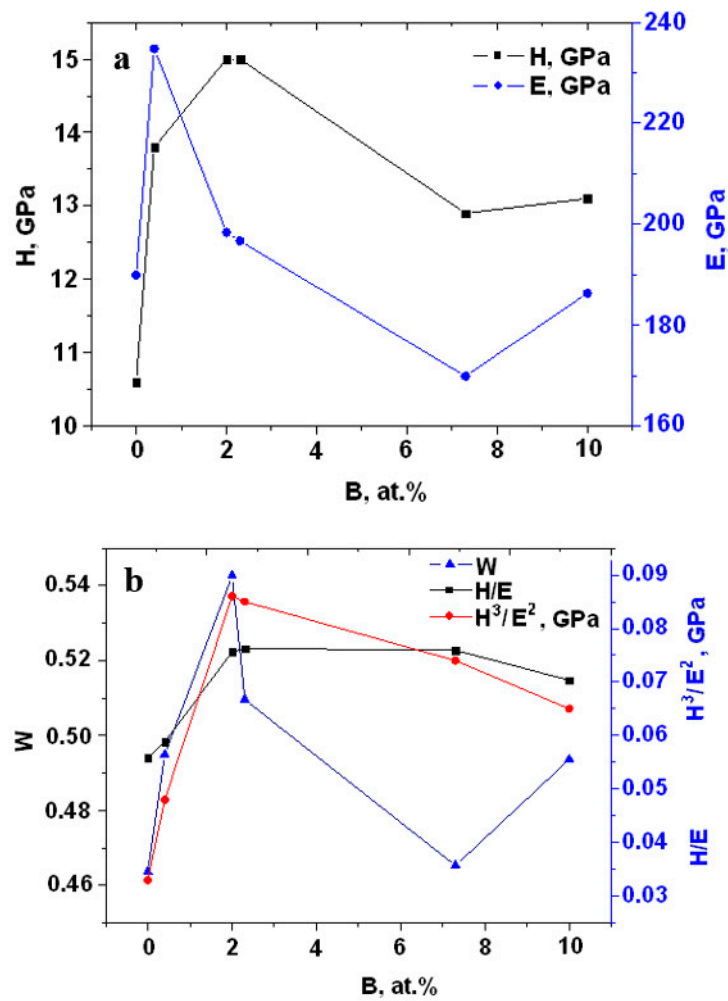


Figure 4. The mechanical (a) and elastic-plastic (b) properties of coatings as a function of boron content.

Wear distance-related plot of friction coefficient for Cr–Al–Ti–B–N coatings (Figure 5) demonstrates that the lowest friction coefficient ( $f = 0.48$ ) was achieved for P3 coating with 2 at.% boron. However, the friction was unstable, and after 90 m distance, the coefficient rose to 0.68–0.7. Boron-free coating P1 had a friction coefficient of 0.8 and suffered complete wear at 135 m. The coatings with the highest boron content demonstrated a drastic increase in friction coefficient (up to 0.8–0.9) during the first 20–30 m. Coating P4 with 2.3 at.% boron, which was characterized by max hardness, demonstrated a stable coefficient  $f = 0.65$ . This coating was the most wear-resistant and endured up to 200 m wear testing without complete wearing-out.

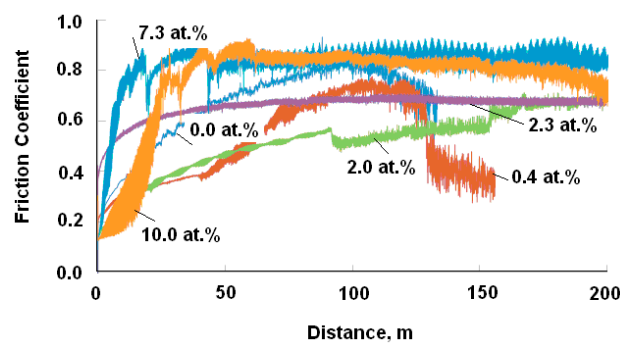
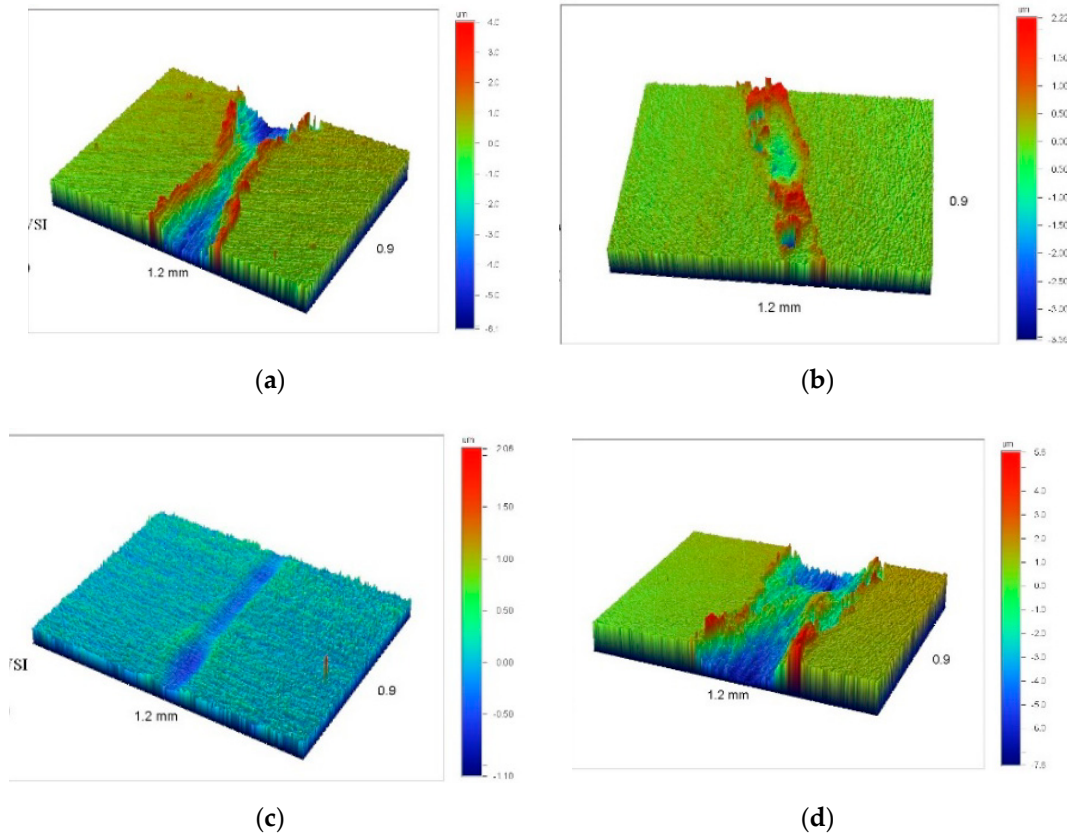


Figure 5. The plot of friction coefficients versus the wear distance for Cr–Al–Ti–B–N coatings.

3D profiles demonstrate the non-uniformity of the wear tracks (Figure 6). Therefore, the wear rate was calculated as the ratio on lengths of fully worn-out and partially worn-out fragments of the track. This calculation was applied for all coatings except the one with 2.3 at.% B, since its wear track had a constant depth and did not reach the substrate’s surface.



**Figure 6.** 3D profiles of wear tracks for the coatings with varied boron content: (a)—0 at.%; (b)—2 at.%; (c)—2.3 at.%; (d)—10 at.%.

The wear rate (Figure 7) for boron-free coatings was  $8.8 \times 10^{-5} \text{ mm}^3/(\text{N}\cdot\text{m})$ , whereas boron-rich coatings P5 (7.3at.% B) and P6 (10 at.% B) had wear rates of  $6.9 \times 10^{-5} \text{ mm}^3/(\text{N}\cdot\text{m})$  and  $1.9 \times 10^{-3} \text{ mm}^3/(\text{N}\cdot\text{m})$ , correspondingly. P4 coating with 2.3 at.% B had the lowest wear rate of  $7.5 \times 10^{-6} \text{ mm}^3/(\text{N}\cdot\text{m})$ .

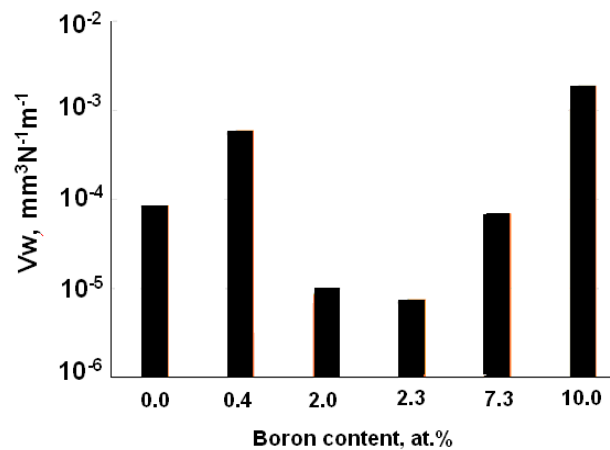


**Figure 7.** Specific wear of Cr–Al–Ti–B–N coatings.

2D and 3D images of the wear tracks (Figure 8) demonstrate that all coatings except coating P4 experience a full wear-out, with the wear track depth exceeding the width of the coatings. In the case of specimen P4, the wear is partial, with the fragments of pristine coatings present along with partially-worn segments. Since the geometrical estimation of wear tracks is unviable, the resistance towards abrasion was estimated by the weight loss during abrasive testing (Figure 9). Maximal weight loss of 0.42 micrograms was recorded for boron-free P1 coating. All boron-containing coatings demonstrated substantially lower weight loss (0.04–0.10 micrograms). The lowest value of 0.04 micrograms was characteristic for P4 coating.

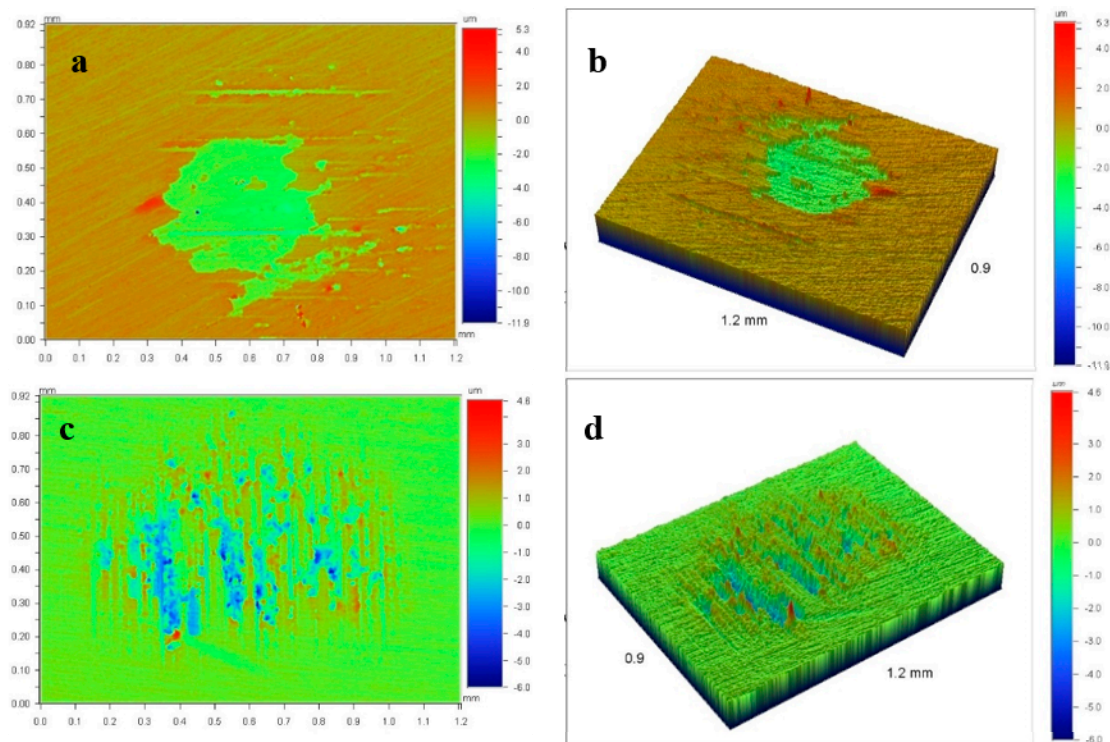


Figure 8. 2D (a,d) and 3D (b,c) profiles of worn zones for coatings with 0 (a,b) and 2.3 (c,d) at.% of boron after the abrasive test.

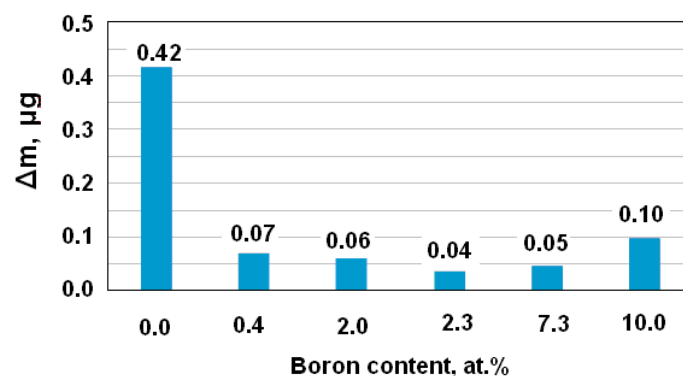
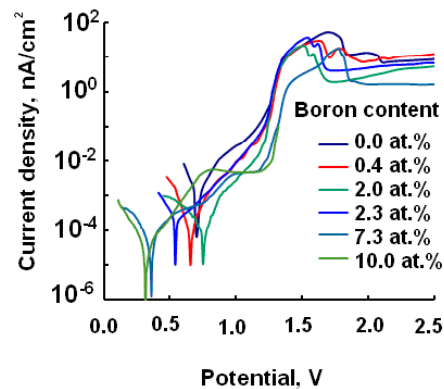


Figure 9. Mass loss after the abrasive test.

The free corrosion potential of coatings in H<sub>2</sub>SO<sub>4</sub> after 30 min exposure was in the 0.310–0.808 V diapason (Table 2). The potential decreased at higher boron content. The initial section of anode polarization curves (Figure 10) is the most characteristic of the coating’s working conditions. The current density (Table 2) was calculated assuming that Ti and Cr are dissolved in solution mainly as the bivalent ions.

**Table 2.** Electrochemical characteristics.

Specimen	B, at. %	U, V	Corrosion Current, nA/cm <sup>2</sup>
P1	0	0.808	140
P2	0.4	0.725	22
P3	2	0.660	18
P4	2.3	0.650	27
P5	7.3	0.330	36
P6	10	0.310	39

**Figure 10.** The plot of current densities versus the free corrosion potential.

For the Cr–Al–Ti–N coating, the max current density was  $\sim 140$  nA/cm<sup>2</sup>. The introduction of boron even in minimal quantities results in a 10-fold decrease in the current density. The minimal density of 18 nA/cm<sup>2</sup> was achieved for the coating with 2.3 at.% B. An increase of boron content to 7–10 at.% yields a 1.5–2 times increase in the current density as compared to 2.3 at.% B.

The second part of the work was dedicated to the development of the upper decorative Cr–Al–Ti–B–O–N layer. Data on the chemical compositions, width, and coloration of the layers are summarized in Table 3. Figures 11 and 12 provide photos of coated specimens. Oxygen content of 0–8 at.% produces a yellow or grey color, whereas 25–40% oxygen in the upper layer produces blue and violet coloration (oxygen content measured by GDOES).

**Table 3.** Deposition parameters, composition, width and coloration of Cr–Al–Ti–B–O–N coatings.

Specimen	$Q_{Air}/Q_{air}$ , cm <sup>3</sup> /min	$\tau$ , min	Elemental Composition, at. %							Coating Thickness, $\mu$ m	Coloration
			Cr	Al	Ti	B	N	O	C		
D1	5/40	10	27.2	5.2	13.8	5.1	16.7	27.4	4.6	0.04	Violet
D2	5/40	20	22.7	3.8	13.8	3.9	11.5	40.2	4.1	0.07	Light-blue
D3	5/40	30	46.7	19.6	13.9	10.4	5.6	2.9	0.9	0.7	Rose
D4	30/30	10	37.5	11.5	8.4	5.9	29.8	6.4	0.5	0.2	Gray
D5	30/30	20	14.7	2.7	13.3	6.8	11.0	40.8	10.7	0.5	Dark-blue
D6	30/30	30	33.4	11.4	11.3	8.5	30.4	4.1	0.9	0.6	Gray
D7	15/30	10	37.9	10.8	8.4	5.7	29.3	7.2	0.7	0.4	Gray
D8	15/30	20	40.0	11.2	9.0	6.2	28.2	4.9	0.5	0.5	Yellow
D9	15/30	30	36.8	11.9	9.2	6.3	31.2	4.2	0.4	1.3	Hazel

As a proof of concept, two-layered coatings were deposited on brass pendants. The lower layer (P) serves protective purposes, whereas the upper layer (D) is decorative. Figure 11 provides photos of pendants before the deposition, after the deposition of the P layer and with a final P + D two-layered coating.

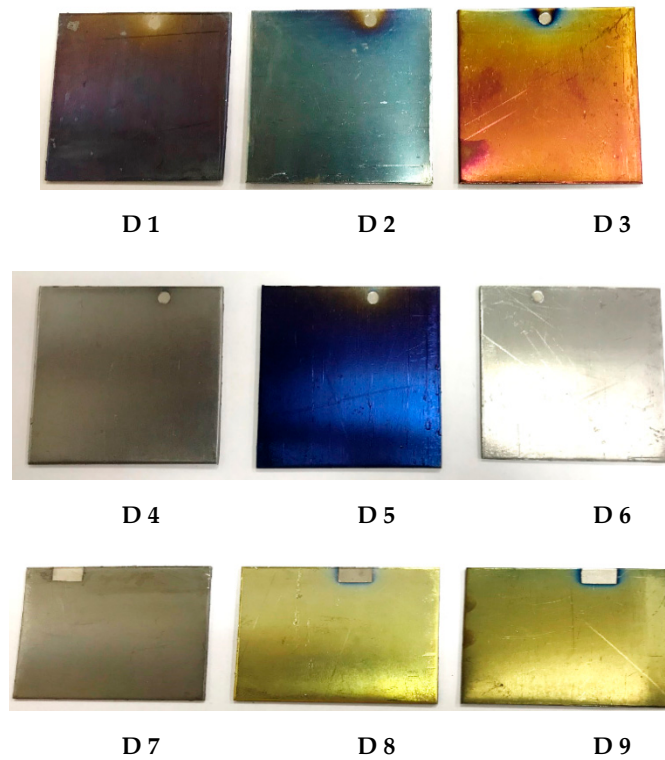


**Figure 11.** Decorative Cr–Al–Ti–B–O–N coatings on SS substrates. Specimens denotation (D1–D9) corresponds with the compositions in Table 3.



**Figure 12.** Uncoated brass pendants (a); pendants with Cr–Al–Ti–B–N coating deposited in P4 mode (b); pendants with Cr–Al–Ti–B–O–N coatings deposited in D5 and D3 modes (c).

#### 4. Discussion

GDOES data reveals the presence of minor amounts of oxygen (5 at.%) and carbon (0.5 at.%) in the Cr–Al–Ti–B–N coatings. Presumably, these impurities originate from residual gas in the deposition

chamber as well as from impurities in working gas and SHS targets. The depth-derived coating growth rate was 30 nm/min.

Boron-free coatings were characterized by columnar growth of the FCC phase and high surface roughness, which are both detrimental for the coating's mechanical properties and performance [45]. The introduction of boron inhibits the formation of columnar grains of chromium and titanium nitrides due to the deformation of their crystal lattices, the prolific formation of crystallization centers, and formation of boron-based thin interlayers (BN or CrB<sub>x</sub>).

The chemical composition of the coatings (Table 1) suggests that chromium nitride should be the main constituting phase. The shift of CrN peaks in XRD patterns is presumably caused by the dissolution of Al atoms in the CrN lattice [46]. Since the atomic radius of Al (0.125 nm) is somewhat lower than that of Cr (0.14 nm), the dissolution of Al in CrN lattice decreases its lattice parameter. The same effect leads to decreasing the lattice parameter of the TiN phase. Boron-based phases were not detected in coatings with 0–2.3 at.% B either because the B amount was insufficient for the precipitation of the related phases or because the content of borides was below the detection threshold of the XRD method. Coatings with 7.3 at.% B were amorphous, so the peaks of discrete phases could not be discerned. A further increase of boron content to 10 at.% evidently leads to the formation of the fine-grained CrB<sub>2</sub>-based phase. The XRD-based estimation of grains size was impossible due to the overlapping peaks; however, the refinement of the structure of CrN-based coatings by boron doping is evident.

Mechanical testing revealed that the coatings containing 2 and 2.3 at.% B possess the highest hardness and elastic-plastic characteristics. It should be noted that both the mechanical properties of boron-containing and boron-free coatings were partially compromised by the deliberate use of low deposition currents—a sacrifice made to prevent the brass substrates from overheating. However, it should be noted that even in the case of sub-optimal deposition conditions, the boron-containing quinary film was considerably more mechanically advantageous (hardness 15 GPa as compared to ~10 GPa in the base coating). One can reasonably expect that at higher sputtering currents, the mechanical properties of the quinary film would rise accordingly. Hardness often defines the wear resistance of bulk materials; in the case of coatings, the  $H/E$  ratio provides a more accurate estimate than the hardness alone [47].  $H^3/E^2$  ratio is characteristic of the type of localized deformation [48]. According to these ratios, the P3 and P4 coatings were the most promising in terms of their wear resistance. This supposition was then confirmed by tribological testing.

The friction coefficient of P3 coating containing c 2 at.% B was unstable and rose gradually due to the local wear. Coatings with max boron content (10 at.%) demonstrated a drastic rise of friction coefficient due to complete wear. The initial friction coefficient of all boron-rich coatings was similar, but the discrepancy arose once the coatings were worn enough for the counter-body to touch the substrate. Coating with 2.3 at.% B endured the wear up to 200 m, presumably due to its higher mechanical and elastic-plastic properties. The abrasion resistance of this coating was also the highest among the investigated ones. A pronounced correlation exists between the hardness (Figure 4) and abrasive resistance (Figure 9) of the coatings.

Relatively low corrosion potentials for the coatings with 7.3 and 10 at.% B suggest direct contact between the solution and some metallic phase (presumably, Cr). Chromium was used as an interlayer between the substrate and the coating and could be exposed as a result of the delamination of coating from the substrate due to high mechanical strains produced by the deformed crystal lattices of coating's constituting phases. The difference in corrosion potentials of coatings with varied boron content is related to the different ratios of nitride and boride phases. The potential of zero currents almost coincides with the free corrosion potential measured without polarization, suggesting that the experimental conditions are close to stationary. At low anode polarization values, the smallest dissolution currents are characteristic for coatings with 0–2.3 at.% B content, whereas the coatings P5 and P6 with exposed Cr interlayers experience an expected faster deposition. A further increase of potential in 1–1.3 V diapason prompted an activation current peak related to the competing dissolution

of titanium and chromium from the corresponding nitrides and related current rise. As the oxide film forms and passivates the coating, the current declines despite the rise of potential. In this stage, the difference in coating composition comes into play. Coatings with higher titanium nitride content demonstrate lower anode dissolution currents, whereas boron-rich coatings dissolve more easily.

An important aspect of this work was the application of segmented planar ceramic SHS targets. These targets can be conveniently used for the industrial-scale deposition of heat-resistant [49,50], wear-resistant [51], corrosion-resistant [52], resistive [53], optically-transparent [39], or antifriction [54] boron-doped coatings.

However, further compositional optimization regarding the content of individual elements might be necessary to realize the optimal properties of the developed multicomponent coating, suggesting directions for future work.

## 5. Conclusions

Cr–Al–Ti–B–N and Cr–Al–Ti–B–O–N coatings were produced for the first time by closed field unbalanced magnetron sputtering using planar TiB SHS targets (STIM-4). The increase of current applied to the TiB target from 0 to 5 A results in an increase of B content in the coating from 0 to 10 at.%, inhibition of columnar growth, densification of coating's microstructure, and surface smoothing. The highest combination of mechanical (hardness 15 GPa; Young modulus 197 GPa; elastic recovery 0.5; elastic deformation of destruction  $H/E = 0.076$ ; resistance against plastic deformation  $H^3/E^2 = 0.085$  GPa) and tribological properties (friction coefficient 0.65, specific wear  $7.5 \times 10^{-6}$  mm<sup>3</sup>/(N·m)) was attained for the coatings containing 2.3 at.%. The relations between deposition parameters, composition, and coloration of coatings were established.

The developed coatings might find a use for the protection of mechanical components from corrosion, abrasion, and wear. The ability to regulate the coloration of the upper layer by altering the oxygen content is particularly useful for the protection or finishing of various works of art since the materials employed in art usually do not allow for any substantial heating.

**Author Contributions:** P.V.K.-K.—supervision, deposition, investigation, and writing the manuscript. Z.S.A.—deposition and testing, writing of the manuscript, A.N.S.—corrosion study, S.V.—translation, correction, and revision of the manuscript. E.A.L.—material support (SHS-target).

**Funding:** This research was funded by the Russian Foundation for Basic Research (RFBR) grant No 19-08-00187.

**Conflicts of Interest:** Authors declare no conflict on interests.

## References

1. Holubář, P.; Jílek, M.; Šíma, M. Nanocomposite nc-TiAlSiN and nc-TiN–BN coatings: Their applications on substrates made of cemented carbide and results of cutting tests. *Surf. Coat. Technol.* **1999**, *120–121*, 184–188. [[CrossRef](#)]
2. Holzschuh, H. Deposition of Ti–B–N (single and multilayer) and Zr–B–N coatings by chemical vapor deposition techniques on cutting tools. *Thin Solid Films* **2004**, *469*, 92–98. [[CrossRef](#)]
3. Kiryukhantsev-Korneev, F.V.; Shirmanov, N.A.; Sheveiko, A.N.; Levashov, E.A.; Petrzhik, M.I.; Shtanskii, D.V. Nanostructural wear-resistant coatings produced on metal-cutting tools by electric-arc evaporation and magnetron sputtering. *Russ. Eng. Res.* **2010**, *30*, 910–920. [[CrossRef](#)]
4. Mitterer, C.; Holler, F.; Üstel, F.; Heim, D. Application of hard coatings in aluminium die casting—Soldering, erosion and thermal fatigue behaviour. *Surf. Coat. Technol.* **2000**, *125*, 233–239. [[CrossRef](#)]
5. Stoiber, M.; Badisch, E.; Lugmair, C.; Mitterer, C. Low-friction TiN coatings deposited by PACVD. *Surf. Coat. Technol.* **2003**, *163*, 451–456. [[CrossRef](#)]
6. He, J.; Miyake, S.; Setsuhara, Y.; Shimizu, I.; Suzuki, M.; Numata, K.; Saito, H. Improved anti-wear performance of nanostructured titanium boron nitride coatings. *Wear* **2001**, *249*, 498–502. [[CrossRef](#)]
7. Berger, M.; Hogmark, S. Tribological properties of selected PVD coatings when slid against ductile materials. *Wear* **2002**, *252*, 557–565. [[CrossRef](#)]

8. Pierson, J.-F.; Chapusot, V.; Billard, A.; Alnot, M.; Bauer, P. Characterisation of reactively sputtered Ti–B–N and Ti–B–O coatings. *Surf. Coat. Technol.* **2002**, *151*, 526–530. [[CrossRef](#)]
9. Lin, S.T.; Lee, C. Characteristics of sputtered Ta–B–N thin films as diffusion barriers between copper and silicon. *Appl. Surf. Sci.* **2006**, *253*, 1215–1221. [[CrossRef](#)]
10. Vlček, J.; Steidl, P.; Kohout, J.; Čerstvý, R.; Zeman, P.; Prokšová, Š.; Perina, V. Hard nanocrystalline Zr–B–C–N films with high electrical conductivity prepared by pulsed magnetron sputtering. *Surf. Coat. Technol.* **2013**, *215*, 186–191. [[CrossRef](#)]
11. Aouadi, S.; Debessai, M.; Namavar, F.; Wong, K.; Mitchell, K. Titanium boron nitride films grown by ion beam assisted deposition: Chemical and optical characterization. *Surf. Coat. Technol.* **2004**, *183*, 369–377. [[CrossRef](#)]
12. Anjum, F.; Fryauf, D.M.; Gold, J.; Ahmad, R.; Cormia, R.D.; Kobayashi, N.P. Study of optical and structural properties of sputtered aluminum nitride films with controlled oxygen content to fabricate Distributed Bragg Reflectors for ultraviolet A. *Opt. Mater.* **2019**, *98*, 109405. [[CrossRef](#)]
13. Shtansky, D.V.; Petrzhik, M.I.; Bashkova, I.A.; Kiryukhantsev-Korneev, F.V.; Sheveiko, A.N.; Levashov, E.A. Adhesion, friction, and deformation characteristics of Ti-(Ca,Zr)-(C,N,O,P) coatings for orthopedic and dental implants. *Phys. Solid State* **2006**, *48*, 1301–1308. [[CrossRef](#)]
14. Sheftel, E.N.; Harin, E.V.; Tedzhetov, V.A.; Kiryukhantsev-Korneev, P.V.; Levashov, E.A.; Perov, N.S.; Titova, A.O. Magnetic structure and magnetic properties of nanocrystalline and amorphous Fe–Zr–N films. *Phys. B Condens. Matter* **2016**, *494*, 13–19. [[CrossRef](#)]
15. Choy, K. Chemical vapour deposition of coatings. *Prog. Mater. Sci.* **2003**, *48*, 57–170. [[CrossRef](#)]
16. Weber, M.; Iatsunskiy, I.; Coy, E.; Miele, P.; Cornu, D.; Bechelany, M. Novel and Facile Route for the Synthesis of Tunable Boron Nitride Nanotubes Combining Atomic Layer Deposition and Annealing Processes for Water Purification. *Adv. Mater. Interfaces* **2018**, *5*, 1800056. [[CrossRef](#)]
17. Snure, M.; Paduano, Q.; Hamilton, M.; Shoaf, J.; Mann, J.M. Optical characterization of nanocrystalline boron nitride thin films grown by atomic layer deposition. *Thin Solid Films* **2014**, *571*, 51–55. [[CrossRef](#)]
18. Weber, M.; Coy, E.; Iatsunskiy, I.; Yate, L.; Miele, P.; Bechelany, M. Mechanical properties of boron nitride thin films prepared by atomic layer deposition. *CrystEngComm* **2017**, *19*, 6089–6094. [[CrossRef](#)]
19. Teer, D. Magnetron Sputter Ion Plating. U.S. Patent No. 5556519A 17 September 1996.
20. Teer, D. Technical note: A magnetron sputter ion-plating system. *Surf. Coat. Technol.* **1989**, *39*, 565–572. [[CrossRef](#)]
21. Kelly, P.J.; Arnell, R.D. Magnetron sputtering: A review of recent developments and applications. *Vacuum* **2000**, *56*, 159–172. [[CrossRef](#)]
22. Arslan, E.; Efeoglu, I. Effect of heat treatment on TiN films deposited by CFUBMS. *Mater. Charact.* **2004**, *53*, 29–34. [[CrossRef](#)]
23. Yao, S.H.; Su, Y.L.; Kao, W.H. Effect of Ag/W addition on the V<sub>war</sub> performance of CrN coatings prepared by RF unbalanced magnetron sputtering. *Mater. Sci. Eng.* **2005**, *25*, 88–92. [[CrossRef](#)]
24. Zhang, F.; Yan, S.; Yin, F.; He, J. Microstructures and mechanical properties of Ti–Cr–N/Al–Ti–Cr based coatings prepared by plasma nitriding 5083 Al alloys co-deposited with Ti–Cr films. *Vacuum* **2018**, *157*, 115–123. [[CrossRef](#)]
25. Kabir, M.S.; Munroe, P.; Zhou, Z.; Xie, Z. Scratch adhesion and tribological behavior of graded Cr/CrN/CrTiN coatings synthesized by closed-field unbalanced magnetron sputtering. *Wear* **2017**, *380–381*, 163–175. [[CrossRef](#)]
26. Xu, J.; Li, Z.; Xie, Z.H.; Munroe, P. Uniting superhardness and damage-tolerance in a nanosandwich-structured Ti–B–N coating. *Scr. Mater.* **2014**, *74*, 88–91. [[CrossRef](#)]
27. Lu, Y.H.; Shen, Y.G.; Zhou, Z.F.; Li, K.Y. Effects of B content and wear parameters on dry sliding wear behaviors of nanocomposite Ti–B–N thin films. *Wear* **2007**, *262*, 1372–1379. [[CrossRef](#)]
28. Ma, Q.; Zhou, F.; Gao, S.; Wu, Z.; Wang, Q.; Chen, K.; Zhou, Z.; Li, L.K. Lawrence Kwok-Yan Li. Influence of boron content on the microstructure and tribological properties of Cr–B–N coatings in water lubrication. *Appl. Surf. Sci.* **2016**, *377*, 394–405. [[CrossRef](#)]
29. Kiryukhantsev-Korneev, F.V.; Petrzhik, M.I.; Sheveiko, A.N.; Levashov, E.A.; Shtanskii, D.V. Effect of Al, Si, and Cr on the thermal stability and high-temperature oxidation resistance of coatings based on titanium boronitride. *Phys. Met. Metallogr.* **2007**, *104*, 167–174. [[CrossRef](#)]

30. Kiryukhantsev-Korneev, F.V.; Novikov, A.V.; Sagalova, T.B.; Petrzhik, M.I.; Levashov, E.A.; Shtansky, D.V. A comparative study of microstructure, oxidation resistance, mechanical, and tribological properties of coatings in Mo–B–(N), Cr–B–(N) and Ti–B–(N) systems. *Phys. Met. Metallogr.* **2017**, *118*, 1136–1146. [[CrossRef](#)]
31. Karvankova, P.; Veprek-Heijman, M.G.J.; Azinovic, D.; Veprek, S. Properties of superhard nc-TiN/a-BN and nc-TiN/a-BN/a-TiB<sub>2</sub> nanocomposite coatings prepared by plasma induced chemical vapor deposition. *Surf. Coat. Technol.* **2006**, *200*, 2978–2989. [[CrossRef](#)]
32. Lee, J.W.; Chih-Hong, C.; Chen, H.W.; Ho, L.W.; Duh, J.G.; Chan, Y.C. The influence of boron contents on the microstructure and mechanical properties of Cr–B–N thin films. *Vacuum* **2013**, *87*, 191–194. [[CrossRef](#)]
33. Kiryukhantsev-Korneev, P.V.; Pierson, J.F.; Bychkova, M.Y.; Manakova, O.S.; Levashov, E.A.; Shtansky, D.V. Comparative Study of Sliding, Scratching, and Impact-Loading Behavior of Hard CrB<sub>2</sub> and Cr–B–N Films. *Tribol. Lett.* **2016**, *63*, 44. [[CrossRef](#)]
34. Budna, K.P.; Mayrhofer, P.H.; Neidhardt, J.; Hegedüs, É.; Kovács, I.; Tóth, L.; Pécz, B.; Mitterer, C. Effect of nitrogen-incorporation on structure, properties and performance of magnetron sputtered CrB<sub>2</sub>. *Surf. Coat. Technol.* **2008**, *202*, 3088–3093. [[CrossRef](#)]
35. Budna, K.; Neidhardt, J.; Mayrhofer, P.; Mitterer, C.; Mayrhofer, P. Synthesis–structure–property relations for Cr–B–N coatings sputter deposited reactively from a Cr–B target with 20at% B. *Vacuum* **2008**, *82*, 771–776. [[CrossRef](#)]
36. Cheng, C.H.; Lee, J.W.; Ho, L.W.; Chen, H.W.; Chan, Y.C.; Duh, J.G. Microstructure and mechanical property evaluation of pulsed DC magnetron sputtered Cr–B and Cr–B–N films. *Surf. Coat. Technol.* **2011**, *206*, 1711–1719. [[CrossRef](#)]
37. Sakamaoto, Y.; Nose, M.; Mae, T.; Honbo, E.; Zhou, M.; Nogi, K. Structure and properties of Cr–B, Cr–B–N and multilayer Cr–B/Cr–B–N thin films prepared by r.f.-sputtering. *Surf. Coat. Technol.* **2003**, *174*, 444–449. [[CrossRef](#)]
38. Zhou, M.; Nose, M.; Nogi, K. Influence of nitrogen on the structure and mechanical properties of r.f.-sputtered Cr–B–N thin films. *Surf. Coat. Technol.* **2004**, *183*, 45–50. [[CrossRef](#)]
39. Kiryukhantsev-Korneev, P.V.; Pierson, J.F.; Petrzhik, M.I.; Alnot, M.; Levashov, E.A.; Shtansky, D.V. Effect of nitrogen partial pressure on the structure, physical and mechanical properties of CrB<sub>2</sub> and Cr–B–N films. *Thin Solid Films* **2009**, *517*, 2675–2680. [[CrossRef](#)]
40. Jahodova, V.; Ding, X.Z.; Seng, D.H.; Gulbinski, W.; Louda, P. Mechanical, tribological and corrosion properties of CrBN films deposited by combined direct current and radio frequency magnetron sputtering. *Thin Solid Films* **2013**, *544*, 335–340. [[CrossRef](#)]
41. Wang, Q.; Zhou, F.; Callisti, M.; Polcar, T.; Kong, J.; Yan, J. Study on the crack resistance of CrBN composite coatings via nano-indentation and scratch tests. *Alloys Compd.* **2017**, *708*, 1103–1109. [[CrossRef](#)]
42. Lua, Y.H.; Zhou, Z.F.; Sit, P.; Shen, Y.G.; Li, K.Y.; Chen, H. X-Ray photoelectron spectroscopy characterization of reactively sputtered Ti–B–N thin films. *Surf. Coat. Technol.* **2004**, *187*, 98–105. [[CrossRef](#)]
43. Lin, J.; Moore, J.; Moerbe, W.; Pinkas, M.; Mishra, B.; Doll, G.; Sproul, W. Structure and properties of selected (Cr–Al–N, TiC–C, Cr–B–N) nanostructured tribological coatings. *Int. J. Refract. Met. Hard Mater.* **2010**, *28*, 2–14. [[CrossRef](#)]
44. Kiryukhantsev-Korneev, P.V.; Phiri, J.; Gladkov, V.I.; Ratnikov, S.N.; Yakovlev, M.G.; Levashov, E.A. Erosion and Abrasion Resistance, Mechanical Properties, and Structure of the TiN, Ti–Cr–Al–N and Cr–Al–Ti–N Coatings Deposited by CFUBMS. *Prot. Met. Phys. Chem. Surf.* **2019**, *55*, 913–923. [[CrossRef](#)]
45. Wu, Z.T.; Qi, Z.B.; Zhang, D.F.; Wei, B.B.; Wang, Z.C. Evaluating the influence of adding Nb on microstructure, hardness and oxidation resistance of CrN coating. *Surf. Coat. Technol.* **2016**, *289*, 45–51. [[CrossRef](#)]
46. Lin, J.; Mishra, B.; Moore, J.J.; Sproul, W.D. Microstructure, mechanical and tribological properties of Cr<sub>1–x</sub>Al<sub>x</sub>N films deposited by pulsed-closed field unbalanced magnetron sputtering (P-CFUBMS). *Surf. Coat. Technol.* **2006**, *201*, 4329–4334. [[CrossRef](#)]
47. Leyland, A.; Matthews, A. On the significance of the H/E ratio in V<sub>war</sub> control: A nanocomposite coating approach to optimised tribological behaviour. *Wear* **2000**, *246*, 1–11. [[CrossRef](#)]
48. Levashov, E.A.; Petrzhik, M.I.; Shtansky, D.V.; Kiryukhantsev-Korneev, P.V.; Sheveyko, A.N.; Valiev, R.Z.; Gunderov, D.V.; Prokoshkin, S.D.; Korotitskiy, A.V.; Smolin, A.Y. Nanostructured titanium alloys and multicomponent bioactive films: Mechanical behavior at indentation. *Mater. Sci. Eng.* **2013**, *570*, 51–62. [[CrossRef](#)]

49. Kiryukhantsev-Korneev, P.V.; Iatsyuk, I.V.; Shvindina, N.V.; Levashov, E.A.; Shtansky, D.V. Comparative investigation of structure, mechanical properties, and oxidation resistance of Mo-Si-B and Mo-Al-Si-B coatings. *Corros. Sci.* **2017**, *123*, 319–327. [[CrossRef](#)]
50. Kiryukhantsev-Korneev, F.V.; Lemesheva, M.V.; Shvyndina, N.V.; Levashov, E.A.; Potanin, A.Y. Structure, Mechanical Properties, and Oxidation Resistance of ZrB<sub>2</sub>, ZrSiB, and ZrSiB/SiBC Coatings. *Prot. Met. Phys. Chem. Surf.* **2018**, *54*, 1147–1156. [[CrossRef](#)]
51. Kiryukhantsev-Korneev, P.V.; Pierson, J.F.; Kuptsov, K.A.; Shtansky, D.V. Hard Cr–Al–Si–B–(N) coatings deposited by reactive and non-reactive magnetron sputtering of CrAlSiB target. *Appl. Surf. Sci.* **2014**, *314*, 104–111. [[CrossRef](#)]
52. Shtansky, D.V.; Kiryukhantsev-Korneev, P.V.; Sheveyko, A.N.; Kutuyev, A.E.; Levashov, E.A. Hard tribological Ti–Cr–B–N coatings with enhanced thermal stability, corrosion- and oxidation resistance. *Surf. Coat. Technol.* **2007**, *202*, 861–865. [[CrossRef](#)]
53. Levashov, E.A.; Kosayanin, V.I.; Krukova, L.M.; Moore, J.J.; Olson, D.L. Structure and properties of Ti-C-B composite thin films produced by sputtering of composite TiC-TiB<sub>2</sub> targets. *Surf. Coat. Technol.* **1997**, *92*, 34–41. [[CrossRef](#)]
54. Shtansky, D.V.; Sheveyko, A.N.; Sorokin, D.I.; Lev, L.C.; Mavrin, B.N.; Kiryukhantsev-Korneev, P.V. Structure and properties of multi-component and multilayer TiCrBN/WSex coatings deposited by sputtering of TiCrB and WSe<sub>2</sub> targets. *Surf. Coat. Technol.* **2008**, *202*, 5953–5961. [[CrossRef](#)]



© 2019 by the authors. Licensee MDPI, Basel, Switzerland. This article is an open access article distributed under the terms and conditions of the Creative Commons Attribution (CC BY) license (<http://creativecommons.org/licenses/by/4.0/>).